A THREE DIMENSIONAL FEM-SIMULATION OF THE SELECTIVE LASER SINTERING PROCESS WITH LOCALLY REFINED MESHES AND NON-CONSTANT THERMAL CONDUCTIVITY.

E. BOILLAT [1], S.KOLOSSOV and R.GLARDON

Institute for Production and Robotics, Laboratory for Production Management and Process, EPFL, CH-1015 Lausanne, Switzerland

A fully three-dimensional Finite Element analysis based on the continuous media theory is used to predict the temperature evolution and the formation of the part during the selective laser sintering process. We consider the modification of the thermal coefficients (like the thermal conductivity and the heat capacity) which is due to temperature changes and phase transformations. We get a quite complex numerical problem, but we can show that the growth in computational time may be partially compensated by the use of finite element meshes with local refinement.

1. Introduction

The subject of this paper is the modelling and the numerical simulation of the Selective Laser Sintering process (SLS). The SLS technology is used to build up three-dimensional parts out of a metallic (or ceramic or plastic) powder. The part is constructed layer by layer by selectively consolidating the powder thanks to a controlled laser-beam.

The main physical phenomena involved in the SLS process as well as their strong interplay mechanisms are not well understood. A systematic regulation of the SLS process is therefore not possible and operators have to rely on long and costly trial and error procedures. The basic motivation of our work is to improve the situation and to propose new alternatives for the process control. Our first goal is to provide a physical insight of the SLS process so that we can get reliable models. The second objective is to tune the SLS process with a "virtual" machine based on numerical simulation. A practical application of the virtual machine would be to test different sets of operating parameters (scanning strategy, laser power, pulse duration, pulse frequency ...) when they are applied to different powders (Aluminium, Titanium or Steel powder) with different grain sizes (from 50 to only a few microns). The long term objective of our study is finally to develop a smart computer-aided tool to optimise the process parameters for getting good parts with minimum input from the operator.

Many references to modelling and numerical simulation of the SLS process can be found in the literature (see [4], [15], [9], [2], [10], [5], [7] or [14]). An essential novelty of our work is to deal with a three-dimensional geometry in an evolutive context. In comparison, the thermal diffusion in the transversal directions is neglected and the global problem is turned into a collection of independent 1D problems in reference [4]. In references [15] and [7], the space dimension is reduced to two under rough symmetry hypotheses. To get pseudo-stationary equations similar to the Rosenthal's equation, the authors of [2] limit their analysis to extremely simple scanning strategy. The modelling of the SLS process we propose in section 2 is based on the continuous media theory. The standard Finite Element Method (FEM) is then chosen for solving the governing equations. For accuracy reason, the FEM mesh size to be used has to be smaller than the radius of the laser beam ($\simeq 100\mu m$). Otherwise the fine features of the scanning strategy would not be correctly reproduced. Since the typical dimensions of the computing domain are of some tenths of centimetres, simulating the evolutive SLS process in a three-dimensional geometry leads to a complex numerical problem reaching the limits of current computers. To compensate the growth in complexity, we will only refine the FEM meshes locally by means of a non-conforming technique. This method will be extensively described in sections 3.2, 3.3 and 3.4. Its efficiency will also be discussed and the accuracy of its predictions will be demonstrated in section 4.

[1]E-mail: eric.boillat@epfl.ch

For a comprehensive description of the medium undergoing sintering, two fields are used in all the aforementioned references: the temperature T and the density ρ. A novelty of our approach is to introduce a third field called "sintering potential". It essentially measures the volume of the necks which build up between particles during sintering. Its main interest is to complete the information contained in the pair of independent variables (T, ρ) for a better description of the conductivity properties of the powder bed. Under the same temperature and for the same density, it has actually been observed that a powder may have different thermal diffusivity, depending on the type of bounds connecting grains.

The third original feature of our work concerns the way phase transitions in the powder bed are taken into account. The melting and resolidification phenomena as well as the changes in crystalline structure significantly impact the laser sintering process. A careful description of these mechanisms is therefore necessary to ensure accurate predictions. Unfortunately, the modelling of phase transitions results in an uncontrolled growth of the heat capacity C_p. For first order phase transitions, the heat capacity actually behaves like the Dirac distribution with an amplitude corresponding to the latent heat. The consequence is that common explicit methods for integrating the temperature evolution cannot be applied anymore. They all are known to require bounded heat capacity to be stable. To overcome this difficulty, we integrate the evolution equations by means of a non-standard scheme based on the Chernoff formula (see [8]). This technique is described in section 3.1. It has the major advantage of being numerically stable even if C_p fails to be bounded from above.

To conclude this introduction, let us stress that our work is mostly focused on the sintering of metallic powders. Most of the topics could however be easily transposed to ceramic or plastic powders as well.

We now proceed with the modelling section.

2. Modelling

Our description of the powder bed under selective laser sintering is based on the mechanics of continuous media. We neglect the phenomena due to mechanical strains and we assume that the chemical composition of the powder is given and does not evolve in time. An elementary model can then be derived by just considering the temperature T, the density ρ, the specific enthalpy u and a fourth variable called sintering potential Φ. It typically measures the quality of the necks between particles build up during sintering.

The four describing fields are space and time depending functions defined on $\Omega \times [0, t_f]$ where $\Omega \in \mathbb{R}^3$ is the sintered media and where t_f represents the total duration of the sintering experiment. The **initial** state (when $t = 0$) of these fields is known and the modelling reduces to find a system of four equations governing their evolution.

The first equation is an algebraic relation between temperature and volume enthalpy. It reads

$$T = \beta(u) \tag{2.1}$$

where β is a non-decreasing and real-valued function of $u \in \mathbb{R}$. The quantity $\frac{1}{\beta'}$ is the specific heat C_p. Since the chemical composition of the powder is known, C_p can be computed as a function of T from experimental data available in tables. A straightforward processing leads then back to a tabulation of $\beta(u)$

Remark 2.1. *For any material, the heat capacity is always bounded from below:*

$$C_p(T) \geq C_p^{min} > 0.$$

Consequently, the derivative of the function β has a bound from above:

$$\beta'(u) = \frac{1}{C_p(\beta(u))} \leq \frac{1}{C_p^{min}}$$

On the other hand, observe that β' has no positive bound from below and can be arbitrarily close to zero as soon as phase transitions are taken into account. The classical example is a first order phase transition at temperature T_0 with latent heat $L > 0$. It implies that $\beta \equiv T_0$ and that $\beta' \equiv 0$ over a whole interval of the form $[u_0, u_0 + L]$.

The temperature evolution is governed by a diffusion equation. Since we are dealing with metallic powders and as the light penetration depth in metals is quite small, we can assume that there are no internal heat sources and the equation for T reads

$$\partial_t \rho u - \mathrm{div} k \nabla T = 0 \tag{2.2}$$

where the thermal conductivity k is a known function of the state variables T, ρ an Φ:

$$k = k(T, \rho, \Phi).$$

Following an idea by Frenkel (see [6]), one can get an evolution law for the density by balancing the viscous dissipation mechanisms in the molten powder and the capillary effects. The relation which is obtained is of the form

$$\partial_t \rho = a(\rho_{solid} - \rho). \tag{2.3}$$

It anticipates an exponential growth of ρ until the value of the solid density ρ_{solid}. The coefficient a is non-negative. It depends on the viscosity of the molten powder and on the surface tension coefficients between the different phases.

Remark 2.2. *The increase in density leads to volumic shrinkage. For the sake of simplicity, the model we are presenting neglects this mechanism. We thus assume that the sintered medium always occupies the same domain Ω.*

In sintering experiments, it can be observed that the volume of necks between particles are approximately proportional to the time spent by the sample above a given temperature T_s. The evolution equation we use for the sintering potential Φ is in agreement on this remark. It reads

$$\partial_t \Phi = \begin{cases} b & \text{if } T > T_s, \\ 0 & \text{if } T \leq T_s. \end{cases} \tag{2.4}$$

The proportionality constant b and the threshold temperature T_s are material depending properties which have to be adjusted from experimental data.

The four equations (2.1)-(2.4) are not sufficient to characterise the medium evolution. The heat flux along the boundary Σ of the sintered domain Ω still needs to be prescribed. Recall that the heat flux along Σ is related to the temperature field by Fourier's law: $-k\partial_n T$ where k is the thermal conductivity and $\partial_n T$ the outward normal derivative of the temperature. Denoting by κ the thermal exchange coefficient between the powder and its environment at ambient temperature T_{amb}, we write the following boundary condition all along Σ:

$$-k\partial_n T - \kappa(T_{amb} - T) = Q. \tag{2.5}$$

The right-hand side Q represents the energy input of the laser beam. It vanishes everywhere except in the part of Σ scanned by the laser. In this region, the value of Q is computed by multiplying the laser intensity (in W/mm^2!) by the absorption coefficient of the powder bed.

3. Numerical resolution

3.1. **Time discretisation.** We choose a time step $\tau > 0$, we set $t_m = m\tau$, $m = 0, 1, 2 \ldots$ and we have to compute approximations T^m, u^m, ρ^m and Φ^m for the profiles of the different fields at time t_m. The profiles T^0, u^0, ρ^0 and Φ^0 at time $t_0 = 0$ are imposed by the initial conditions and the basic idea is to combine the evolution equations (2.1)-(2.5) for designing a reasonable procedure which leads to the profiles at time t_m when their values are known at time t_{m-1}.

Updating ρ^m and Φ^m by using the ordinary differential equations (2.3) and (2.4) is a straightforward operation. We thus can focus on the integration method to be used for deducing T^m and u^m from T^{m-1}, u^{m-1}, ρ^{m-1} and Φ^{m-1}. Applying the Chernoff formula (see [8]) to the algebraic-differential equations (2.1)-(2.2) completed by the boundary condition (2.5) yields

$$\rho^m(u^m - u^{m-1}) - \tau \mathrm{div} k^{m-1} \nabla T^m = 0, \text{ in } \Omega, \tag{3.1}$$

$$-k^{m-1}\partial_n T^m - \kappa(T_{amb} - T^m) = Q^m, \quad \text{on } \Sigma, \tag{3.2}$$

$$T^m = \beta(u^{m-1}) + \omega(u^m - u^{m-1}), \tag{3.3}$$

In the system (3.1)-(3.3), $\omega > 0$ is a stabilisation parameter and k^{m-1} is the thermal conductivity computed at the previous time layer:

$$k^{m-1} = k(T^{m-1}, \rho^{m-1}, \Phi^{m-1}).$$

The advantage of the scheme (3.1)-(3.3) is to provide approached profiles T^m and u^m which converge to the exact profiles under a simple condition on the stabilising parameter ω (see [8]). This condition is connected with the minimum value C_p^{min} of the powder heat capacity (see Remark 2.1). It reads

$$\omega \geq \frac{1}{C_p^{min}}.$$

In comparison, the Euler-forward method (which corresponds to the particular choice $\omega = 0$) would not converge at all while other methods would require a bound from below for β'. Unfortunately, such a bound does not exist if phase transitions are taken into account (see Remark 2.1).

3.2. **Space discretisation.** The equation (3.3) has to be interpreted as an explicit relation for the enthalpy profile,

$$u^m = u^{m-1} + \frac{T^m - \beta(u^{m-1})}{\omega}, \tag{3.4}$$

and (3.1)-(3.2) can be transformed in a boundary value problem for the temperature profile T^m. It reads

$$cT^m - \mathrm{div} a \nabla T^m = f, \quad \text{in } \Omega, \tag{3.5}$$

$$-a\partial_n T^m + \lambda T^m = g, \quad \text{on } \Sigma \tag{3.6}$$

by way of the obvious identifications $c = \rho^m$, $a = \omega\tau k^{m-1}$, $f = \rho^m \beta(u^{m-1})$, $\lambda = \omega\tau\kappa$ and $g = \omega\tau(\kappa T_{amb} + Q^m)$. Since we mean to find a FEM approximation of the profile T^m, we have to write the problem (3.5)-(3.6) in a variational form:

$$\alpha(T^m, v) = l(v) \tag{3.7}$$

for any continuous and piecewise differentiable test function v. In the formulation (3.7) the bilinear form α and the linear form l are connected to the data c, a, f, λ and g by the classical definitions (see e.g. [12])

$$\alpha(u, v) = \int_\Omega (cuv + a\nabla u \cdot \nabla v) d\omega + \int_\Sigma \lambda uv d\sigma \text{ and } l(v) = \int_\Omega fv d\omega + \int_\Sigma gv d\sigma. \tag{3.8}$$

The finite element mesh is designed carefully according to the laser location. We divide the computation domain Ω in two parts, Ω_c and Ω_f with interface Γ:

$$\Omega = \Omega_c \cup \Omega_f \cup \Gamma.$$

The domain Ω_c is supposed to stay far away from the region scanned by the laser and it is meshed by coarse cells to limit the numerical complexity of the problem (the subscript c in Ω_c stands for coarse). On the other hand, we equip the domain Ω_f, where the laser activity is confined, with fine cells (the subscript f in Ω_f stands for fine). For accuracy reasons, the typical size h of the fine cells has to be smaller than the radius of the laser beam. The

novelty of our approach is that the sub-domains Ω_c and Ω_f are meshed independently. The meshing and remeshing procedures are therefore very simple and the fine grid can easily be transported to follow the path of the laser beam at each time step. An example of the situation is represented in Figure 1.

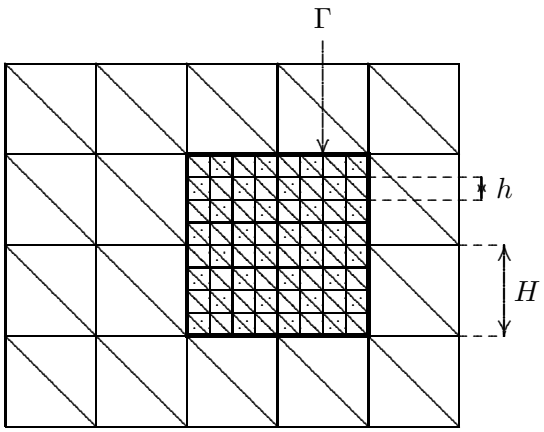

FIGURE 1. A view from above of the mesh. The dashed region corresponds to the domain Ω_f.

In general and as it can be observed in Figure 1, the element do not satisfy the standard compatibility constraint (see [12]) along the interface Γ. This is the reason why our FE method requires a non standard formulation. It is exposed in the next paragraph.

3.3. **The FE formulation.** We first have to introduce the notations $\mathcal{M}_c$, $\mathcal{M}_f$ and, respectively, $\mathcal{M} = \mathcal{M}_c \cup \mathcal{M}_f$ for the meshes in Ω_c, in Ω_f and for the resulting mesh in Ω. The FE space will be called V. It contains all the piecewise linear functions over $\mathcal{M}$ which are continuous *separately* in Ω_c and in Ω_f. Observe that the functions in V are not necessarily continuous across the interface Γ. This fact will be exploited in the implementation phase of the FEM (see paragraph 3.4). The approximation T_h^m of the temperature profile T^m will be searched in V. In the standard Galerkin method, T_h^m is defined as the element of V which is *continuous* across Γ and which satisfies the variational formulation (3.7) for any *continuous* test function $v \in V$. Unfortunately, imposing the continuity of the temperature T_h^m across Γ in an explicit way leads to a complicated discrete problem. This problem has the saddle point structure and can be ill-conditioned. To avoid this situation, we have decided to penalise the continuity constraint across Γ.

For this purpose, we introduce the notation N_i, $1 \leq i \leq n$, for the nodes belonging to the coarse mesh $\mathcal{M}_c$ and located on the interface Γ. To each node N_i, we associate a jump operator c_i. It is defined on the space V by the relation

$$c_i(v) = v_{|\Omega_f}(N_i) - v_{|\Omega_c}(N_i), \, \forall \, v \in V. \tag{3.9}$$

The penalty technique can now be expressed. We choose a small penalty parameter $\varepsilon > 0$ and we define the approached temperature profile T_h^m as the element in V satisfying

$$\alpha(T_h^m, v) + \frac{1}{\varepsilon} \sum_{i=1}^{n} c_i(T_h^m) c_i(v) = l(v), \, \forall \, v \in V. \tag{3.10}$$

The bilinear and linear forms α and l in (3.10) are as in (3.7). The convergence properties of the penalty method can be found in [1] and the next paragraph essentially discusses a way to implement it.

3.4. **Implementation of the FEM.** The outputs of the FE computations we are interested in are the values of the approached temperature profile T_h^m at the nodes of the mesh M. We use the notation N_i, $1 \leq i \leq m$ for these nodes. Observe that the n first nodes, $N_1 \dots N_n$, have already been introduced in paragraph 3.3. They were defined as the nodes belonging to the coarse mesh $\mathcal{M}_c$ and located on the interface Γ. Another important feature has to be stressed. If a point $P \in \Gamma$ is a node in $\mathcal{M}_c$ and, simultaneously, a node in $\mathcal{M}_f$, then it has to appear twice in the list $\{N_i\}$: $P = N_i = N_{i'}$ with $i \leq n$ and $i' > n$.

In the sequel, the unknown values of T_h^m at the nodes N_i will be denoted as u_i: $u_i \equiv T_h^m(N_i)$. They will also be considered as the components of a vector $\mathbf{u} = (u_1 \dots u_m) \in \mathbb{R}^m$. Once the $u_i's$ are determined, the profile T_h^m can be recovered by applying the Lagrange formula

$$T_h^m = \sum_{i=1}^{m} u_i \varphi_i \tag{3.11}$$

where φ_i is the shape function associated to the node N_i. Recall that φ_i is defined as the unique element of V vanishing in each node N_j, $j \neq i$, and satisfying $\varphi_i(N_i) = 1$.

Substituting the development (3.11) of T_h^m into the penalised problem (3.10) and choosing the test function v as any of the shape function, we get a linear system for $\mathbf{u}$. It reads

$$(K + \frac{1}{\varepsilon} \sum_{i=1}^{n} \mathbf{c}_i \mathbf{c}_i^t)\mathbf{u} = \mathbf{b} \tag{3.12}$$

where the matrix $K \in M_m(\mathbb{R})$ and the vectors $\mathbf{b}, \mathbf{c}_i \in \mathbb{R}^m$ are connected to the bilinear and linear forms α and l in (3.10) and to the jump operator c_i, defined in (3.9), by some obvious relations which are discussed below.

The matrix K is the *regular* stiffness matrix and $\mathbf{b}$ is the *regular* right-hand side:

$$K_{ij} = \alpha(\varphi_j, \varphi_i),\ 1 \leq i, j \leq m \text{ and } b_i = l(\varphi_i),\ 1 \leq i \leq m. \tag{3.13}$$

In the FE code we have developed, the matrix elements K_{ij} and the components b_i are computed by means of a loop over the elements in Ω and over the faces meshing the surface Σ. The positive definite matrix K is sparse and we use the routines of the *Sparselib* library (see [3]) to store it.

For $1 \leq i \leq n$, the component number j of the constraint vector $\mathbf{c}_i$ is defined by

$$[\mathbf{c}_i]_j = c_j(\varphi_j) = (\varphi_j)_{|\Omega_f}(N_i) - (\varphi_j)_{|\Omega_c}(N_i). \tag{3.14}$$

It follows from (3.14) that $\mathbf{c}_i$ has only four non-zero components. The first one is the component number i. It satisfies

$$[\mathbf{c}_i]_i = -1 \tag{3.15}$$

because φ_i is the shape function associated to the node N_i located in the coarse mesh. To determine the three other non-zero components of $\mathbf{c}_i$, we first locate the node N_i in the fine mesh $\mathcal{M}_f$. This can be done with a standard FE algorithm. It reads the connectivity of the faces in the fine mesh which lie on the interface Γ and it is able to select the particular one which contains N_i. Let N_{k_1}, N_{k_2} and N_{k_3} be the three vertices of that face. Let also ξ and $\eta \in [0, 1]$ be the coefficients such that it holds

$$ON_i = \xi ON_{k_1} + \eta ON_{k_2} + (1 - \xi - \eta) ON_{k_3}.$$

Then we have

$$[\mathbf{c}_i]_{k_1} = \xi, \quad [\mathbf{c}_i]_{k_2} = \eta \quad \text{and} \quad [\mathbf{c}_i]_{k_3} = 1 - \xi - \eta. \tag{3.16}$$

We use (3.13), (3.15) and (3.16) to construct the matrix K and the vectors $\mathbf{b}$ and $\mathbf{c}_i$. We then solve the positive definite system (3.12) by means of the conjugate gradient algorithm (see [3]). The convergence of this method is good provided we pay some attention to design

the penalty parameter ε. Too small values of ε may actually spoil the conditioning of the system (3.12) and slow down the convergence rate of the conjugate gradient algorithm.

4. Some results

In this section we report the results of the simulation of a sintering experiment. The part to be sintered was a ring with inner radius $R_i = 1.25mm$ and outer radius $R_e = 2.5mm$ and the material was Titanium powder.

The thermal conductivity of the Titanium powder is a function of the temperature T and of the sintering potential Φ. It is supposed to be independent of the density ρ. We use an interpolation rule

$$k(T, \Phi) = (1 - \Phi)k_{powder} + \Phi k_{bulk}(T) \tag{4.1}$$

between the thermal conductivity of bulk Titanium and the thermal conductivity of loose Titanium powder. The bulk thermal conductivity, k_{bulk}, is plotted as a function of temperature in Figure 2(a) while the loose powder thermal conductivity, k_{powder}, is assumed to be independent of the temperature. A reasonable value of this quantity can be found in [11]:

$$k_{powder} = 1.5[W/mK].$$

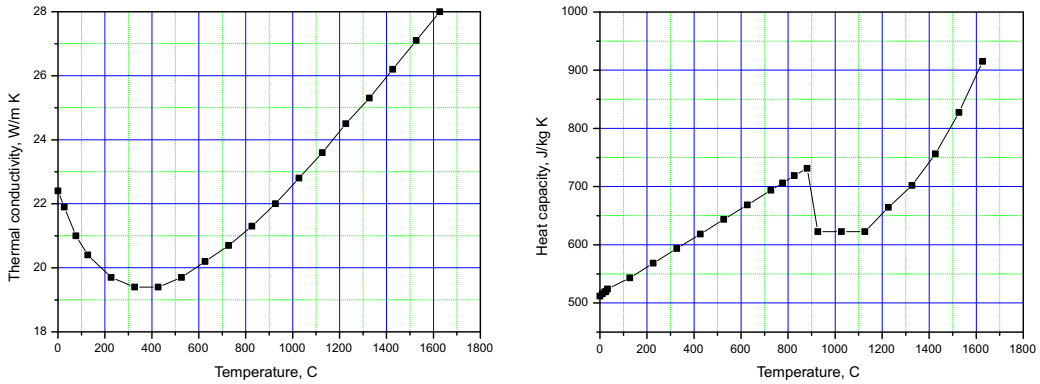

(a) The thermal conductivity. (b) The specific heat.

Figure 2. Thermodynamic properties of the bulk Titanium

Beside the thermal conductivity, the function β, which is characteristic of the thermodynamic properties of Titanium powder, is necessary to write down the evolution equations (2.1) and (2.2) for the temperature and the specific enthalpy. According to the theory developed in section 2, $\beta(u)$ can be obtained by processing the specific heat capacity of the bulk material. This last quantity is represented as a function of the temperature in Figure 2(b).

It has been observed experimentally that the densification mechanisms occurring during the laser sintering of Titanium powder can be neglected. It means that the densification law (2.3) can be simplified by setting $a = 0$. We can also assume that the material density is constant:

$$\rho = 4.5\text{g/cm}^3.$$

The threshold temperature T_s affecting the evolution rate of the sintering potential (see (2.4)) has been chosen equal to the melting temperature of bulk Titanium:

$$T_s = T_{melt} = 1953K.$$

and the unknown coefficient b has been normalised to one.

The description of the experiment is completed by some information about the laser parameters (see Figure 3) and about the laser scanning strategy (see Figure 4).

Variable	Notation	Value	Unit
Average power	P	5.0	$[W]$
Period	t_p	$1.0 * 10^{-2}$	$[s]$
Pulse duration	t_d	$1.0 * 10^{-4}$	$[s]$
Spot radius	R	$2.0 * 10^{-4}$	$[m]$
Laser path length	L	$10.2 * 10^{-2}$	$[m]$
Laser spot speed	S	$4.0 * 10^{-2}$	$[\frac{m}{s}]$
Duration of the laser activity	t_a	2.55	$[s]$

FIGURE 3. The laser parameters.

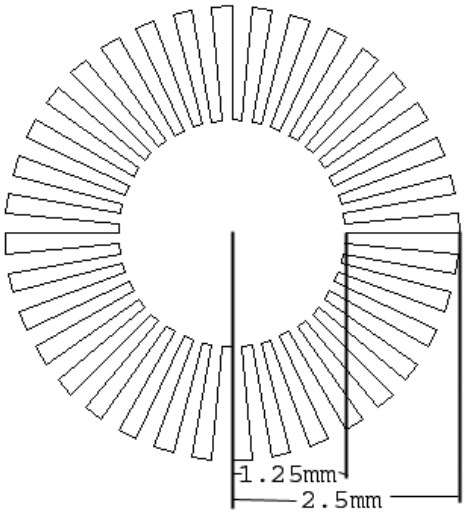

FIGURE 4. The laser scanning strategy

Those informations are used to build the right hand-side in the boundary condition (2.5).

The ring has been manufactured by depositing three successive layers of powder with a thickness of about $L = 50\mu m$. The horizontal dimensions of the working area (corresponding to the computation domain Ω) were

$$l_1 = 10mm \text{ and } l_2 = 10mm$$

We did two different numerical experiments. In the first one, we tried to demonstrate the efficiency of the non-conformal meshing technique described in section 3.2. The goal of the second experiment was to predict the shape of the sintered part.

4.1. **The efficiency of the non-conformal meshing technique.** We performed the same simulation but with two different meshes. The first mesh was uniformly refined all over the computation domain Ω (see Figure 5(a))

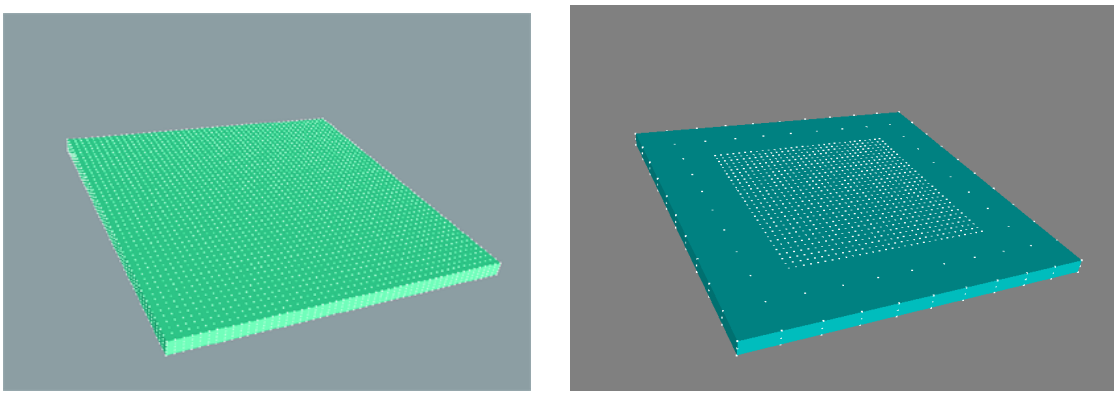

(a) The uniformly refined mesh. (b) The locally refined mesh.

FIGURE 5. The two different meshes.

while the second mesh was only locally refined (see Figure 5(b)) in a central parallelepiped Ω_f with horizontal dimensions

$$l_1' = 6mm \text{ and } l_2' = 6mm$$

We considered the results obtained with the uniformly refined mesh as a reference. Figure 6 represents the evolution of the relative error (in the square gradient norm) which affects the temperature profile computed with the locally refined mesh. In comparison, we also plot the relative error we would get by roughly reducing the computation domain to Ω_f. In that case, we assume that the boundary $\partial\Omega_f$ is an insulating border.

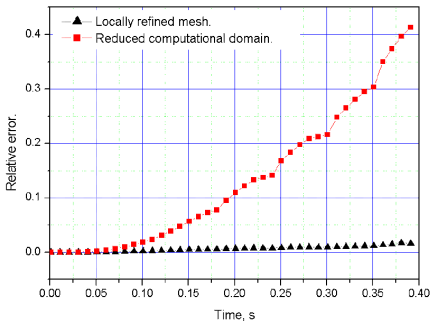

FIGURE 6. The errors due to the refinement technique and to the insulation of Ω_f

The conclusions we can draw from Figure 6 are clear. On the one hand, neglecting the heat transfer across the boundary $\partial\Omega_f$ of the refined domain Ω_f leads to an unacceptable error in the predictions of the temperature profile for large time. On the other hand, the prediction quality of the locally and totally refined meshes are comparable for any time. As a consequence and since it reduces the computation effort by a factor 4, the locally refined mesh is preferable.

4.2. **The shape of the sintered part.** The shape of the sintered part is predicted by processing the final distribution of the sintering potential Φ. We assume that the sintered

region is the domain where the sintering potential has risen above some value Φ_0. We typically choose

$$\Phi_0 = 0.75.$$

The predicted part is represented in Figure 7(a). It can be compared to the sintered sample in Figure 7(b).

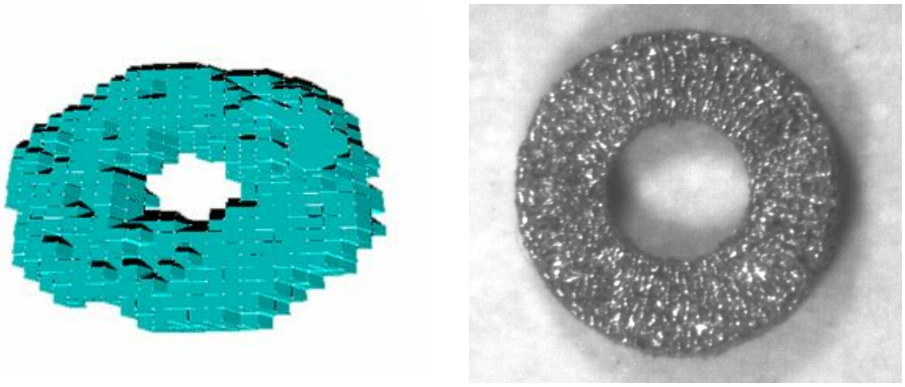

(a) The predicted sintered part. (b) The real sintered part.

FIGURE 7. Comparison between simulation and experiment

A good agreement can be observed between the predicted and the sintered parts. It confirms that the *sintering potential*, evolving according to equation (2.4), is closely connected to the real consolidation level of the powder. Observe however that the parameters in equation (2.4) as well as the value Φ_0, reached by the sintering potential in the consolidated region, need to be carefully adjusted. The main issue which still need to be addressed is the design of relevant experimental setups for fitting those quantities. In the same way, we are considering more sophisticated models of liquid phase sintering (e.g. those which are based on Plateau's problem see [13]) in order to improve the evolution equation for the sintering potential.

REFERENCES

[1] E.Boillat. Finite Element Methods on Non-Conforming Grids by Penalizing the Matching Constraint. submitted for publication to M2AN.

[2] G.Bugeda, M.Cervera, and G.Lombera. Numerical predicton of temperature and density distributions in selective laser sintering process. *Rapid Prototyping Journal*, 5(1):21–26, 1999.

[3] Dongarra J., Lumsdaine A., Pozzo R., and Remington K. A Sparse Matrix Library in C++ for High Performance Architectures. In *Proceedings of the Second Object Oriented Numerics Conference*, pages 214–218, 1992.

[4] J.C.Nelson, S.Xue, J.W.Barlow, J.J.Beaman, H.L.Marcus, and D.L.Bourell. Model of the Selective Laser Sintering of bisphenol-a Polycarbonate. *Ind.Eng.Chem.Res.*, 32:2305–2317, 1993.

[5] Williams J.D and Deckard C.R. Advances in modeling the effects of selected parameters on the SLS process. *Rapid Prototyping Journal*, 4(2):90–100, 1998.

[6] J.Frenkel. Viscous flow of crystalline bodies under the action of surface tension. *J.Phys.USSR*, 9:385–391, 1945.

[7] Matsumoto M., Shiomi M., Osakada K., and Abe F. Finite element analysis of single layer forming on metallic powder bed in rapid prototyping by selective laser processing. *International Journal of Machine Tools & Manufacture.*, 42:61–67, 2001.

[8] E. Magenes, R.H. Nochetto, and C. Verdi. Energy error estimates for a linear scheme to approximate nonlinear parabolic problems. *Mathematical modelling and numerical analysis*, 21(4):655–678, 1987.

[9] M.Berzins, T.H.C.Childs, and G.R.Ryder. The Selective Laser Sintering of Polycarbonate. *Annals of the CIRP*, 45(1):187–190, 1996.

[10] M.Kandis and T.L.Bergmann. A Simulation-Based Correlation of the Density and Thermal Conductivity of Objects Produced by Laser Sintering of Polymer Powder. *Journal of Manufacturing Science and Engineering*, 122:439–444, 2000.

[11] P.Fischer, N.Karapatis, V.Romano, and H.P.Weber. A model for the interaction of near infrared laser pulses with metal powders in selective laser sintering. *Applied physics A*, 74(4):467–474, 2002.

[12] Ciarlet P.G. *The Finite Element Method for Elliptic Problem*. North Holland, Amsterdam, 1978.

[13] P.Salamon, J.Bernholc, R.S.Berry, M.E.Carrera-Patino, and B.Andersen. The wetted solid, a generalization of plateau's problem and its implications for sintered materials. *J.Math.Phys.*, 31:610–615, 1990.

[14] Childs T.H.C., Hauser C., Taylor C.M., and Tontovi A.E. Simulation and experimental verification of crystalline polymer and direct metal selective laser sintering. In D.L. Bourell and al., editors, *Solid Freeform Fabrication Symposium Proceedings*, pages 100–109, 2000.

[15] N.K. Vail, B.Balasurbramanian, J.W. Barlow, and H.L. Marcus. A thermal model of polymer degradation during selective laser sintering of polymer coated ceramic powders. *Rapid Prototyping Journal*, 2(3):24–40, 1996.